TU Delft

Delft University of Technology

Document Version
Final published version

Licence
CC BY

Citation (APA)
Soman, S., Özdemir, E., & Pereira, S. (2026). Scanning in coherent Fourier scatterometry using Fresnel zone plate projection on a digital micro-mirror device. *Measurement Science and Technology*, *37*(15), Article 155002. https://doi.org/10.1088/1361-6501/ae5abc

Important note
To cite this publication, please use the final published version (if applicable).
Please check the document version above.

Copyright
In case the licence states "Dutch Copyright Act (Article 25fa)", this publication was made available Green Open Access via the TU Delft Institutional Repository pursuant to Dutch Copyright Act (Article 25fa, the Taverne amendment). This provision does not affect copyright ownership.
Unless copyright is transferred by contract or statute, it remains with the copyright holder.

Sharing and reuse
Other than for strictly personal use, it is not permitted to download, forward or distribute the text or part of it, without the consent of the author(s) and/or copyright holder(s), unless the work is under an open content license such as Creative Commons.

Takedown policy
Please contact us and provide details if you believe this document breaches copyrights.
We will remove access to the work immediately and investigate your claim.

This work is downloaded from Delft University of Technology.

Measurement Science
and Technology

PURPOSE-LED
PUBLISHING™

PAPER • OPEN ACCESS

Scanning in coherent Fourier scatterometry using Fresnel zone plate projection on a digital micro-mirror device

To cite this article: Sarika Soman *et al* 2026 *Meas. Sci. Technol.* **37** 155002

View the article online for updates and enhancements.

You may also like

- Autler–Townes splitting in Rydberg atoms: transition dipole matrix element extraction and field efficiency analysis
Brian C Holloway, Gavin M Chase, Lee E Harrell et al.

- ICRH modelling of DTT in full power and reduced-field plasma scenarios using full wave codes
A Cardinali, C Castaldo, F Napoli et al.

- Optimized polarization in DUV scatterometry with global sensitivity analysis for accurate CD metrology of sub-micron microstructure structures
Fu-Sheng Yang, Yen-Hung Hung, Min-Ru Wu et al.

This content was downloaded from IP address 154.59.124.113 on 24/04/2026 at 13:16

Measurement Science and Technology

OPEN ACCESS

RECEIVED
19 November 2025

REVISED
18 February 2026

ACCEPTED FOR PUBLICATION
2 April 2026

PUBLISHED
13 April 2026

Original content from this work may be used under the terms of the Creative Commons Attribution 4.0 licence.

Any further distribution of this work must maintain attribution to the author(s) and the title of the work, journal citation and DOI.

PAPER

Scanning in coherent Fourier scatterometry using Fresnel zone plate projection on a digital micro-mirror device

Sarika Soman[1], Eren Özdemir[1,2] and Silvania Pereira[1,*]

[1] Department of Imaging Physics, Delft University of Technology, Lorentzweg 1, 2628 CJ Delft, The Netherlands
[2] The Hague University of Applied Sciences, Rotterdamseweg 137, 2628 AL Delft, The Netherlands
[*] Author to whom any correspondence should be addressed.

E-mail: s.f.pereira@tudelft.nl

Keywords: scatterometry, optical metrology, high-speed scanning

Abstract

We present a digital micro-mirror device (DMD)-enabled scan head for coherent Fourier scatterometry (CFS) that performs lateral scanning without macroscopic moving parts, while maintaining a diffraction-limited probe. A binary Fresnel zone plate (FZP) is displayed and translated on the DMD to steer a single focused spot across the sample, providing an electronically programmable alternative to scanning using piezo-based translation devices. To the best of our knowledge, this is the first published CFS implementation in which a DMD is the primary lateral scanning element. Furthermore, the DMD programmability is used to compensate for the scan-position-dependent aberrations using an iterative optimisation algorithm. Across a 400×200 DMD-pixel scan area, the peak-intensity coefficient of variation improves from 39.4% (uncorrected) to 16.1% (after correction) and to 4.47% with additional power normalisation, demonstrating substantially improved probe uniformity. Finally, we demonstrate particle detection on a Si wafer with 1 μm polystyrene latex particles, achieving an signal-to-noise ratio of 16.04 ± 1.11 dB. The results establish DMD-FZP scanning with integrated aberration correction as a compact, fast, and scalable CFS architecture, with a clear pathway to higher throughput via multi-spot parallelisation.

1. Introduction

The trend of device miniaturisation across fields such as photonics, healthcare and consumer electronics has been aided by the parallel development of tools that can measure and characterise these devices often in the nanoscale regime [1, 2]. Optical metrology tools in particular have become an industry workhorse due to its fast, non-contact measurement techniques that offer good spatial and axial resolution measurements without damaging the sample [3–5].

Coherent Fourier scatterometry (CFS) is an optical metrology technique designed for the non-destructive, high-resolution characterisation of surfaces. It has been used in a wide range of applications, including diffraction grating characterisation [6], nerve crossing detection [7], defect detection on SiC wafer for power electronics [8], and nanoparticle and nanostructure characterisation on Si wafers and plastic substrates [9–11]. CFS uses a focused spot, created using an objective lens, as a probe to scan the sample surface. The reflected light is collected by the same objective and measured using a detector placed in the Fourier plane, i.e. the back focal plane (BFP) of the objective.

The small probe spot enables high spatial resolution, but it must be scanned laterally to generate a two-dimensional scattering map. In conventional CFS setups this is commonly achieved using 2D piezo translation stages. While piezo scanning offers high positioning accuracy and typically low noise, it is slow for large-area scans and requires physical motion of the sample, which makes long scans susceptible to drift. To improve throughput, alternative strategies have been explored, including rotation stages, galvo-mirror beam scanning, and scan-probe multiplexing using diffractive beam splitters [12–14]. Each approach involves distinct trade-offs: beam scanning using galvo-mirror enables high scan speeds but introduces intrinsic field-dependent (off-axis) aberrations and detector-plane beam shifts that vary across

© 2026 The Author(s). Published by IOP Publishing Ltd

Table 1. Comparison of different scanning strategies for a CFS system.

Scanning strategy	Scan time[a]	Pros	Cons
Piezo-based scanning [9]	300 s[b]	Simple optical system; low power; low detection bandwidth requirement; low noise.	Very slow; expensive; long scan time causes drift; unsuitable for in-line measurements.
Galvo mirror-based scanning [14]	1 s	High-speed scanning; relatively inexpensive; single axis scan suitable for roll-to-roll manufacturing.	Angle-dependent optical aberrations; beam shift at detector; high electronic bandwidth requirement.
DMD-based scanning (proposed)	56 s[c]	High-speed scanning; no macroscopic moving parts; optical aberration corrections possible; can be extended to multi-probe design using a single DMD.	Low power efficiency; requires prior system calibration;

[a] Scan time for a 100 µm × 100 µm scan area with 100 nm pixel size.
[b] Scan frequency = 1/35 of the first resonant frequency of the piezo (P-625.2 CD, Physik Instrumente)
[c] Scan time calculated for highest 1-bit refresh rate of 17 857 Hz.

the scan field, while multiplexed approaches increase throughput but suffer from similar angle dependent aberrations and impose stricter alignment and calibration requirements.

In this work, we introduce a digital micro-mirror device (DMD) based scan head for CFS in which the lateral scan is performed electronically by translating a Fresnel zone plate (FZP) pattern displayed on a DMD. DMDs are micro-electromechanical systems comprising a two-dimensional array of individually addressable, bistable micro-mirrors that can switch within microseconds [15]. Because each micro-mirror functions as a binary pixel, a DMD can project arbitrary binary patterns, enabling compact and programmable beam steering and wavefront shaping when incorporated into an appropriate optical relay. These properties have motivated the use of DMDs in a range of imaging and metrology applications, including scanning microscopy [16–18], structured illumination microscopy [19, 20], LiDAR [21, 22], compressed sensing [23, 24], and ptychography [25, 26].

To the best of our knowledge, this is the first published CFS implementation in which a DMD serves as the primary lateral scanning element. The approach occupies a practical middle ground between piezo and galvo-mirror-based beam scanning and probe-multiplexed strategies. It increases throughput relative to piezo-stage scanning while keeping the sample stationary. The DMD programmability also enables scan-position-dependent aberration compensation and output-power normalisation using the same hardware, improving probe uniformity across the scan field. The same framework is directly extensible to multi-probe operation by displaying multiple FZPs in parallel, enabling further throughput scaling without introducing additional beam-steering hardware. Table 1 summarises representative scanning strategies used in CFS and their principal trade-offs.

Lateral scanning across a finite field of view introduces field-dependent aberrations for off-axis focus positions, which degrade probe quality and can introduce scan-position-dependent signals for nominally identical sample features. The DMD programmability can therefore be used not only for scanning but also as an adaptive element for scan-position-dependent wavefront correction. Sensor-less adaptive-optics correction using DMDs has been demonstrated in various imaging contexts [27–35]. In this work, we implement an iterative Zernike-based optimisation to determine a corrective phase to be applied at each scan position, and we quantify the resulting improvement in probe uniformity and stability. The performance of the calibrated and aberration-corrected DMD-based CFS system is demonstrated on particle detection on a Si wafer.

The article is organised as follows: section 2 discusses the basic measurement principle, section 3 describes the experimental setup and scanning parameters, section 4 quantifies system performance and details the aberration-correction implementation, section 5 presents a scan example of contamination detection on a Si wafer, section 6 analyses uncertainty contributions and section 7 concludes with a discussion of the results.

2. Measurement principle

This section summarises the CFS measurement concept, outlines DMD-based scanning options for CFS, and introduces the aberration-correction workflow implemented using the DMD.

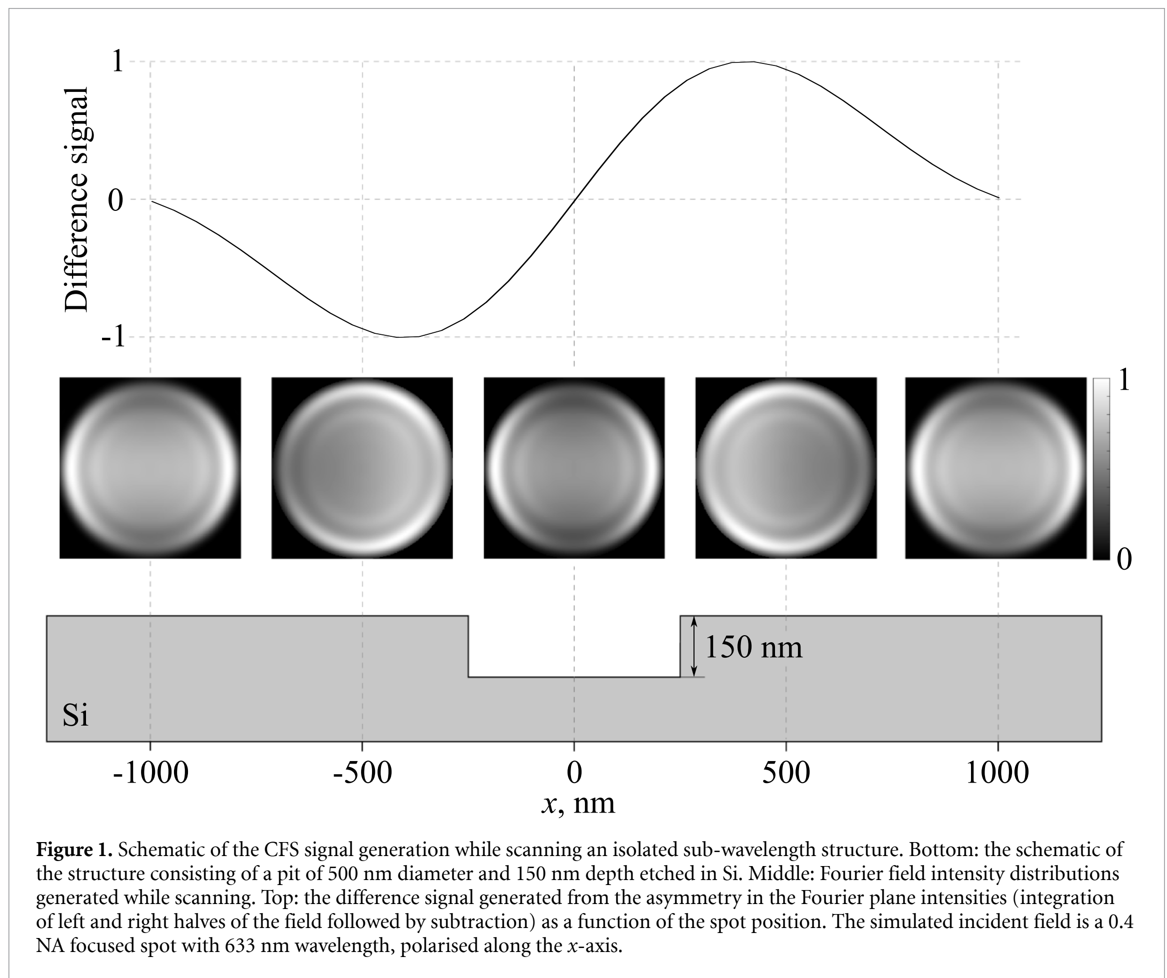

Figure 1. Schematic of the CFS signal generation while scanning an isolated sub-wavelength structure. Bottom: the schematic of the structure consisting of a pit of 500 nm diameter and 150 nm depth etched in Si. Middle: Fourier field intensity distributions generated while scanning. Top: the difference signal generated from the asymmetry in the Fourier plane intensities (integration of left and right halves of the field followed by subtraction) as a function of the spot position. The simulated incident field is a 0.4 NA focused spot with 633 nm wavelength, polarised along the x-axis.

2.1. Coherent Fourier scatterometry (CFS)

CFS is a scatterometry-based metrology technique in which a focused optical probe is scanned across a sample while the angular scattering response is measured in the Fourier plane. In the experimental implementation, an objective lens forms a diffraction-limited spot on the sample and simultaneously collects the reflected/scattered field. The Fourier plane corresponds to the BFP of the objective. Under the scalar Fresnel diffraction approximation, the objective performs a Fourier transform, establishing a direct mapping between position in the BFP and plane-wave propagation direction [36]. The resulting BFP intensity distribution therefore provides an angle-resolved fingerprint of the local sample response.

To illustrate the signal formation, figure 1 shows simulated Fourier-plane intensity distributions obtained while scanning a focused spot along the x-direction across an isolated sub-wavelength pit. As the probe crosses the structure, the Fourier-plane intensity becomes asymmetric, with the strongest changes occurring near the pupil edges. This left–right asymmetry motivates differential readout strategies in which the CFS signal is formed from an intensity difference between two pupil regions (left/right).

2.2. Scanning using a DMD

Scanning in CFS setups using a DMD can be realised in multiple ways. In general, these strategies can be categorised into three groups: (i) single pixel or sub-array scanning [17, 18, 37], (ii) grating projection [38], and iii) FZP / binary lens projection [39–41]. A schematic illustrating the three approaches is shown in figure 2. Each approach has significant advantages and disadvantages.

In the first approach, a single micro-mirror or a small cluster of micro-mirrors on the DMD is sequentially switched on. The cluster is then re-imaged onto the sample to achieve diffraction-limited spots. The approach is easy to implement and can be multiplexed to generate multiple parallel beams, but it suffers from considerable power loss. The second approach involves displaying a series of binary gratings with varying spatial periods. The advantage is that a larger fraction of the beam power is used, reaching up to 7% of the incident power [38]. However, it provides only coarse angular sampling, and the intensity at the scan spot is not constant with steering angle. The first-order power varies with steering angle because the DMD window transmission and the first-order efficiency of the grating depend

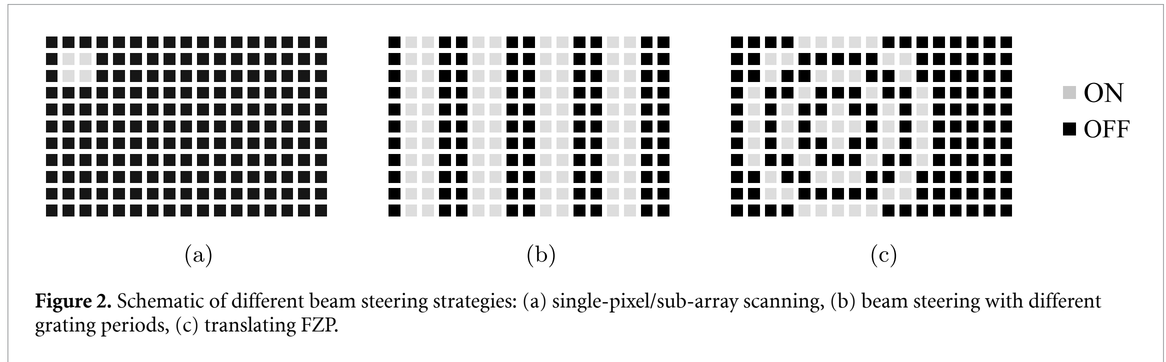

Figure 2. Schematic of different beam steering strategies: (a) single-pixel/sub-array scanning, (b) beam steering with different grating periods, (c) translating FZP.

on angle and polarisation (Fresnel reflections and fill-factor effects) [38]. In the third approach, an FZP translated on the DMD converts a collimated input beam into a movable focal spot, retaining a higher percentage of the input power compared to the first approach, with the efficiency reaching 3.8% [39], while having angle-independent intensity. This scanning approach was chosen as it balances power utilisation and scan-parameter control.

An FZP consists of a series of concentric circular rings with increasing radius, designed to focus an incident plane wave with wavelength λ at a focal length f. The radius of the nth zone boundary is given by [42],

$$r_n = \sqrt{n\lambda f + \frac{n^2\lambda^2}{4}}, \tag{1}$$

which reduces to

$$r_n \approx \sqrt{n\lambda f}, \qquad \text{when } f \gg n\lambda/4. \tag{2}$$

The outermost usable radius r_n is chosen such that the outer ring width matches one micromirror, i.e. $r_n - r_{n-1} = p$, where p is the DMD micromirror pitch. Using $r_n^2 - r_{n-1}^2 = \lambda f$ and $r_n + r_{n-1} \approx 2r_n$ gives

$$r_n = \frac{\lambda f}{2p}, \qquad n = \frac{\lambda f}{(2p)^2}. \tag{3}$$

The moving focused spot after the DMD is relayed to the sample plane using an optics relay. The relay must be chosen such that the minimum step size in the image/sample plane, corresponding to a single micromirror shift in the DMD plane satisfies the Nyquist sampling criterion applied to the highest detectable spatial frequency. Assuming no non-linear effects are present in the interaction of the spot with the sample, the largest spatial frequency of the sample that can be detected is $2\text{NA}/\lambda$, where λ is the wavelength of the coherent source and NA is the numerical aperture of the focusing lens [43–45].

2.3. Aberration correction

Each scan position on the sample plane experiences a slightly different optical path, as a result, the point-spread function (PSF) varies across the field of view. This variability degrades measurement quality because identical structures at different scan coordinates can yield inconsistent signals, increasing measurement uncertainty. A detailed study on the influence of aberrations on the measured CFS signal is detailed in Soman *et al* (2025) [46]. Using the programmability of the DMD, in addition to scanning, the same device can also be used to correct aberrations. For each scan coordinate in the sample plane, a suitable correction phase can be computed and displayed on the DMD, thereby improving PSF uniformity over the entire field of view and reducing measurement uncertainty.

The optimal wavefront correction per position is expressed in a Zernike polynomial basis. Zernike polynomials provide a convenient, orthogonal basis for representing common aberrations such as astigmatism, coma, defocus, and spherical aberration on a circular pupil. An optimisation algorithm, shown schematically in figure 3, is used to find the optimal Zernike coefficients at each scan position. As the DMD can project only binary amplitude modulation, the required phase corrections must first be encoded as binary amplitude patterns [29, 33]. The binary amplitude distribution $A(x,y)$ for each scan position is computed from the desired phase-correction map $\varphi(x,y)$ as

$$A(x,y) = \begin{cases} 1, & \cos\varphi(x,y) > 0, \\ 0, & \text{otherwise}. \end{cases} \tag{4}$$

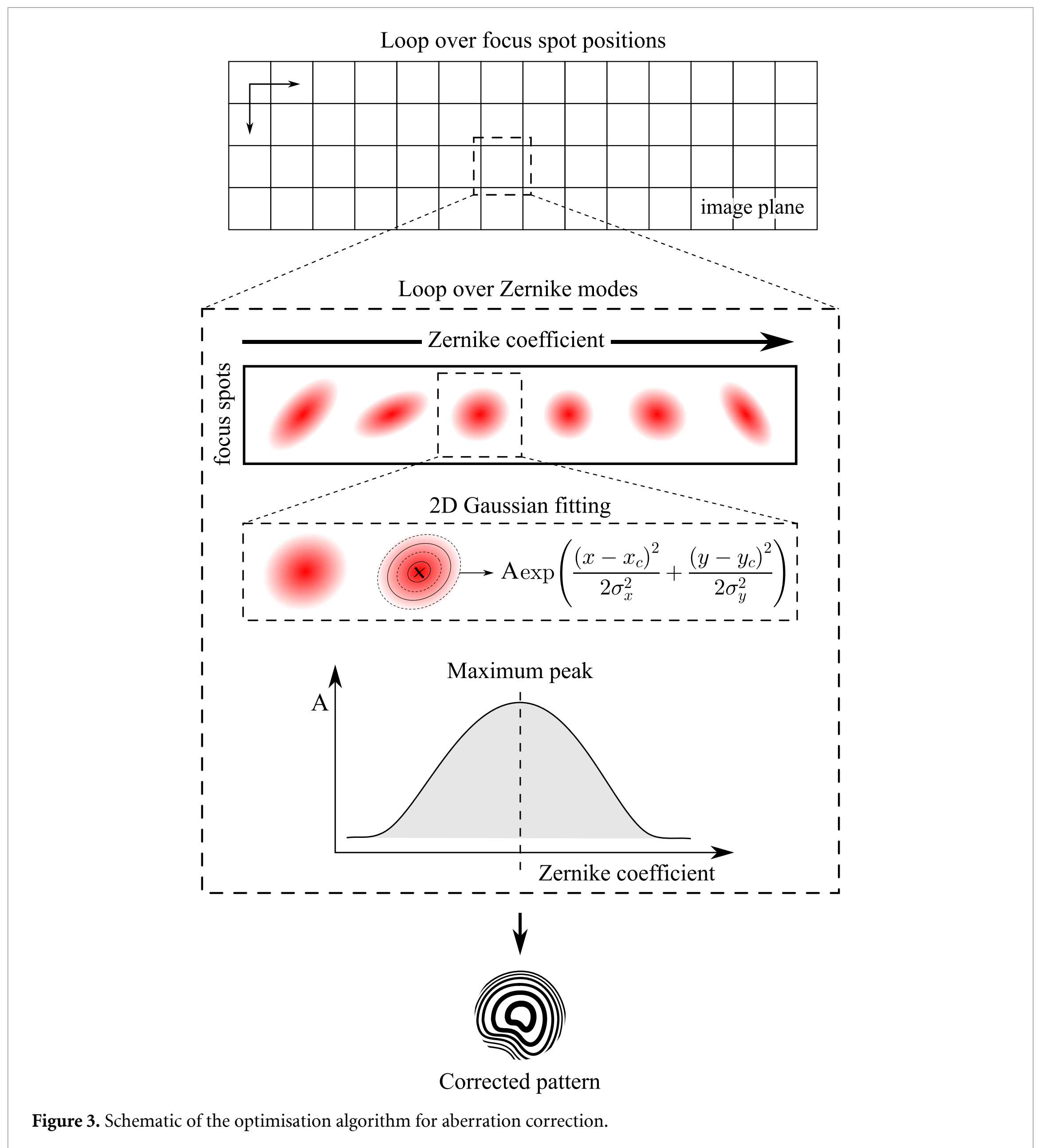

Figure 3. Schematic of the optimisation algorithm for aberration correction.

The specific details of the algorithm used in the setup is detailed in subsection 4.3.

3. Experimental setup

This section details the implementation specific details. The schematic of the experimental setup is shown in figure 4. A HeNe laser (nominal output power 30 mW) with wavelength $\lambda = 632.8$ nm is expanded using lenses L1 ($f = 10$ mm) and L2 ($f = 250$ mm) in a telescopic arrangement, providing a magnification of 25 $\times$. The expanded beam is incident on the DMD (DLP9500, Texas Instruments). Light reflected from the DMD is collimated by L3 ($f = 300$ mm) and then focused onto the sample by the microscope objective (N PLAN L 20×/0.40 NA, Leica). The reflected light from the sample is collected by the same objective. The BFP of the objective is relayed to a quadrant detector (SD 085-23-21-021, Advanced Photonix) using lenses L4 ($f = 250$ mm) and L5 ($f = 50$ mm) forming a 0.2 $\times$ telescope. An additional CCD camera (MER2-160-227U3M, Daheng Imaging) is used to locate areas of interest on the sample. Lenses L4 and L6 ($f = 100$ mm) demagnify the BFP by 0.4 $\times$ before relaying it to the camera. A flip mirror is used to switch between the detector and camera paths. The sample is mounted on a

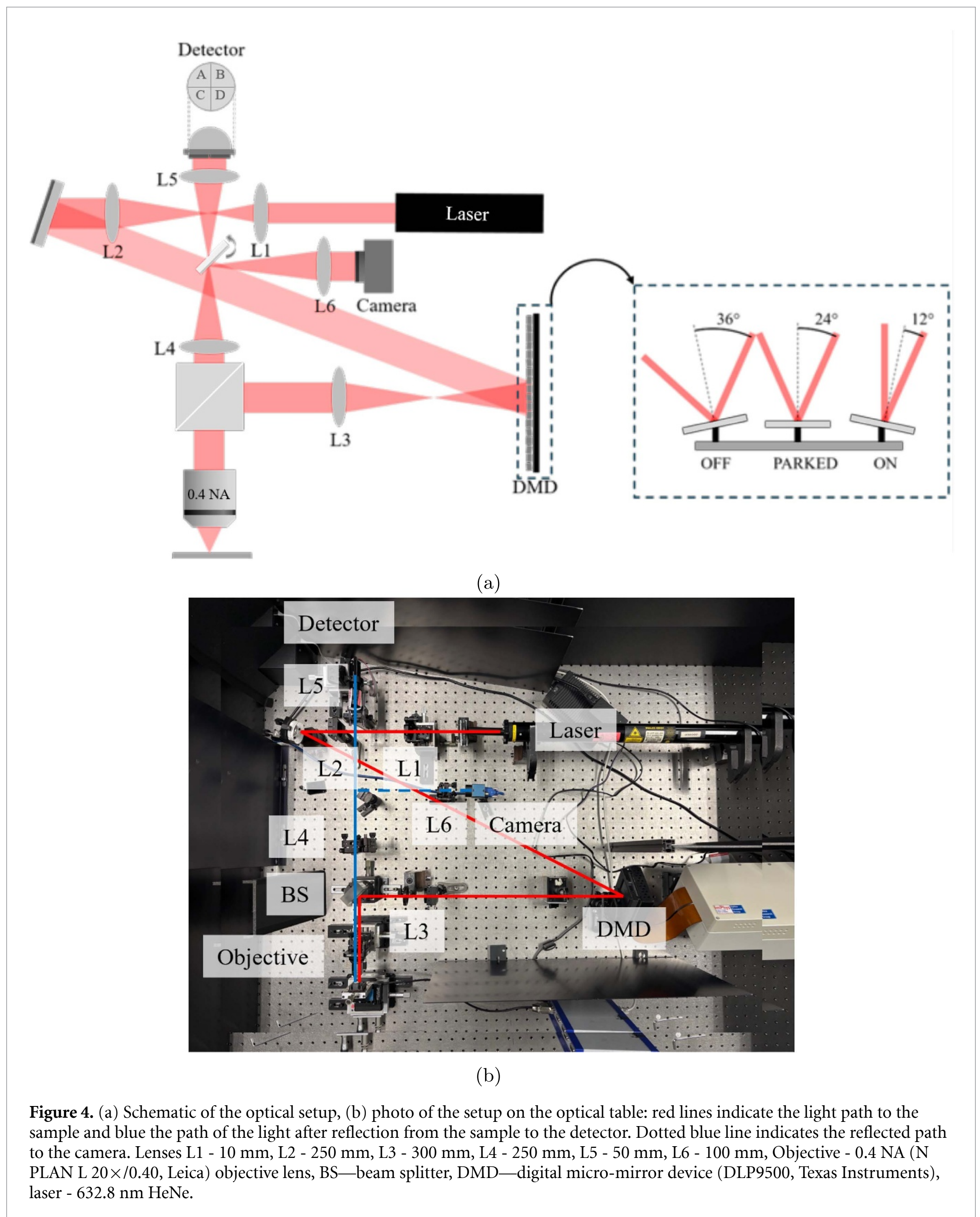

Figure 4. (a) Schematic of the optical setup, (b) photo of the setup on the optical table: red lines indicate the light path to the sample and blue the path of the light after reflection from the sample to the detector. Dotted blue line indicates the reflected path to the camera. Lenses L1 - 10 mm, L2 - 250 mm, L3 - 300 mm, L4 - 250 mm, L5 - 50 mm, L6 - 100 mm, Objective - 0.4 NA (N PLAN L 20×/0.40, Leica) objective lens, BS—beam splitter, DMD—digital micro-mirror device (DLP9500, Texas Instruments), laser - 632.8 nm HeNe.

piezo stage (M-110.12S, Physik Instrumente) for fine focus control along the z-axis. Coarse alignment is provided by manual translation stages along the x-, y- and z-axes.

3.1. DMD

The DMD chip (DLP9500, Texas, USA) has a diagonal of 0.95 inch and contains a rectangular array of 1920 × 1080 micro-mirrors with a pitch of 10.8 µm, resulting in an active area of 20.7 mm × 11.7 mm. The chip is driven by a controller board (V-9501, Vialux GmbH, Germany) capable of frame rates up to 17 857 Hz for 1-bit images. Each mirror consists of a highly reflective aluminium surface attached via a post to compliant torsion hinges that define the rotation axis. When an external voltage is applied, the mirror rotates and latches electrostatically into one of two stable tilt states. In the ON state the mirror tilts by $+12°$ with respect to the substrate normal, in the OFF state it tilts by $-12°$. With no voltage, the mirror remains parallel to the substrate ('PARKED'). Figure 4(a) schematically illustrates the mirror states.

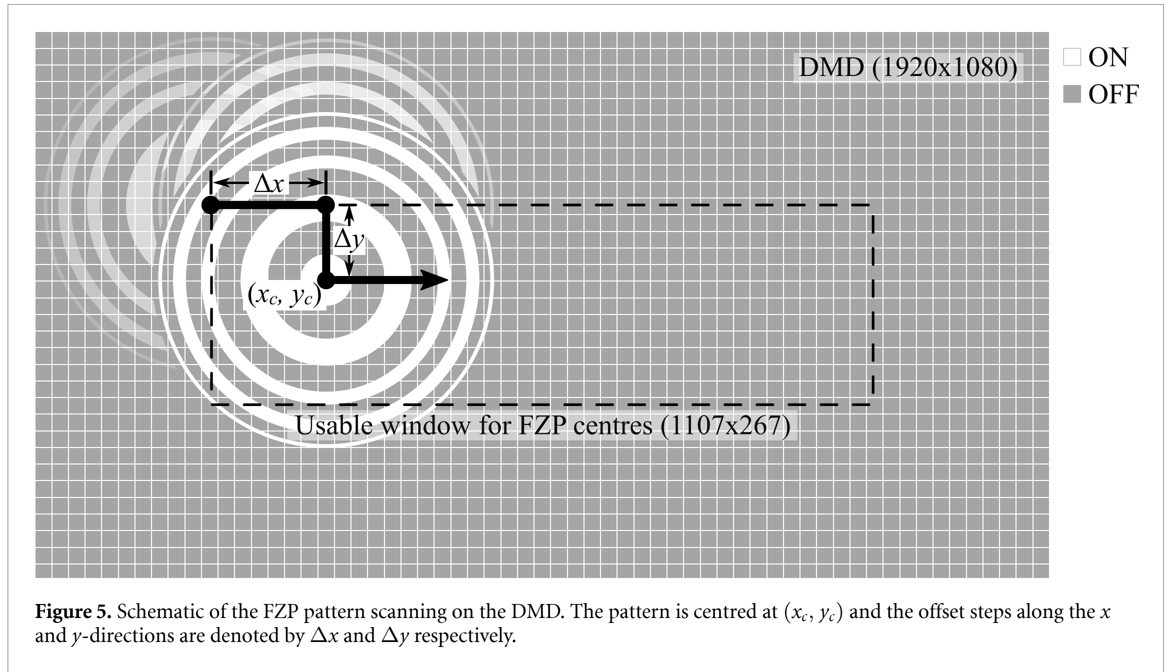

Figure 5. Schematic of the FZP pattern scanning on the DMD. The pattern is centred at (x_c, y_c) and the offset steps along the x and y-directions are denoted by Δx and Δy respectively.

In the configuration of figure 4(b), the input beam is incident on the DMD at 24° relative to the substrate normal so that light from ON pixels is directed along the optical axis of the system. The DMD package is mounted with its substrate normal parallel to the optical axis. Because the torsion hinge lies along the mirror diagonal, the ON/OFF deflections occur in a plane rotated by 45° about the optical axis. Accordingly, the entire DMD is rotated by 45° during mounting so that the reflected beams lie in the horizontal plane of the optical table.

3.2. FZP scanning

The focal length of the FZP projected on the DMD was chosen to 150 mm. For $\lambda = 632.8$ nm, and micromirror pitch $p = 10.8\,\mu$m, the first zone radius r_1 is calculated using figure 3 to be 0.308 mm, corresponding to a first zone diameter of 57 micro-mirrors, i.e. DMD pixels, and $r_n = 4.394$ mm, corresponding to the last zone diameter of 813 micromirrors at $n = 203$.

Figure 5 shows the schematic of the FZP scanning on the DMD. The scanning consists of displaying FZP patterns centred at different (x_c, y_c) positions on the DMD. The lateral shifts along x and y-directions are programmed by Δx and Δy, with a minimum DMD-plane step equal to one micromirror, $\Delta x_{\text{min}} = \Delta y_{\text{min}} = p$. If M is the magnification of the relay between the FZP focal plane and the sample plane, the minimum step-size in the sample plane, $\Delta x_{\text{s,min}}$, is Mp. To avoid cropping the FZP at the device edges, the admissible FZP-centre window is reduced to $(1920 - 813) \times (1080 - 813) = 1107 \times 267$ micromirrors on a 1920×1080 DMD. While scanning, each FZP pattern is projected on the DMD for a duration of $1/f_{\text{DMD}}$, where f_{DMD} corresponds to the refresh rate of the DMD. The unwanted higher diffraction orders are blocked using an aperture placed in the focal plane of the FZP.

The four photodiode outputs (A, B, C, D) from the quadrant detector are digitised simultaneously (NI 9215, ±10 V). Two differential detector signals along two orthogonal directions can be calculated as,

$$D_1 = (A + B) - (C + D) \tag{5}$$

$$D_2 = (A + D) - (B + C)\,. \tag{6}$$

The detector is aligned such that the beam is centred uniformly between the four quadrants.

3.3. Focusing efficiency

The amount of power concentrated in the focus spot can be calculated as [39],

$$\eta_{\text{focus}} = \eta_{\text{FZP}}\,\eta_{\text{circ}}\,\eta_{\text{DMD}} \tag{7}$$

$$= 0.016 \quad (\text{experimentally measured})\,, \tag{8}$$

where,

- η_{focus} is the fraction of total power incident on the DMD that is concentrated in the focus spot of the FZP projection on the DMD,
- $\eta_{FZP} = 1/\pi^2$ is the focusing efficiency of a binary FZP into the first-order focus [39],
- $\eta_{circ} \approx 0.250$ is the fraction of the area covered by the FZP on the DMD,
- $\eta_{DMD} = 0.633$ (experimentally measured) is the overall optical efficiency due to the DMD [47].

$$\eta_{DMD} = \eta^2_{transmission\ window}\,\eta_{fillfactor}\,\eta_{diffraction}\,\eta_{reflectivity}. \tag{9}$$

- $\eta_{transmission\ window}$ is the single-pass window transmission including anti-reflection coatings,
- $\eta_{fillfactor}$ is the fractional mirror coverage,
- $\eta_{diffraction}$ is the mirror array diffraction efficiency which can include effects of non-flat mirrors,
- $\eta_{reflectivity}$ is the mirror reflectivity.

4. System characterisation

This section reports system characteristics relevant to scanning performance: step size, intensity calibration, and position-dependent aberrations.

4.1. Step size measurement

Unlike scanning stages with position sensors for feedback, the beam position during DMD scanning is not directly measured and therefore must be determined experimentally. In practice, this amounts to mapping scan parameters expressed in DMD coordinates to coordinates in the sample (focal) plane. Apart from residual optical distortion, the mapping is a geometric scaling, set by the effective magnification of the relay after the DMD (lens L3 and the objective).

To guarantee sufficient sampling, the Nyquist criterion is applied to the highest spatial frequency of interest. For a system with NA = 0.40 and a wavelength of 632.8 nm, the largest detectable sample spatial frequency is $f_{max} = 1.264\,\mu m^{-1}$. According to the Nyquist criterion,

$$\Delta x_{s,min} \leqslant \frac{1}{2f_{max}} = 0.396\,\mu m,$$

where $\Delta x_{s,min}$ denotes the sample-plane step corresponding to a one-micro-mirror shift on the DMD.

To experimentally determine $\Delta x_{s,min}$, a diffraction grating with a period of 1658 nm and a 50% duty cycle was used. The sample was fabricated and pre-calibrated by partners of the 17FUN01 BeCOMe project. The grating period has been independently measured using a scanning electron microscope. The differential signal obtained while scanning perpendicular to the grating lines is periodic with the same spatial period as the grating. The step size corresponding to one micro-mirror shift is computed directly from the scan data. Figure 6 shows the step-size calculation from the 2D differential data of a grating sample (6(a)). Figure 6(b) shows a profile perpendicular to the grating lines (blue circles) extracted from the 2D data, interpolated profile (black dashed line), and the profile minima marked as red triangles. The separation distance between two consecutive minima corresponds to one grating period. From the data, the step-size corresponding to one micro-mirror shift is measured to be $0.363 \pm 0.008\,\mu m$, which satisfies the Nyquist condition.

The same method was also used to measure the optical distortion in the system. Ideally, the scan grid in the sample plane is a rectilinear mapping of the DMD micro-mirror array. Optical distortion would appear as location-dependent changes in the measured step size. Scans shifted by ±250 micro-mirrors along x resulted in step-sizes of $0.364\,\mu m$ and $0.366\,\mu m$, respectively, both within the $\pm 0.008\,\mu m$ measurement uncertainty, indicating negligible distortion over the tested field of view.

4.2. Intensity variation

After expansion by lenses L1 and L2, the beam incident on the DMD exhibits a low-frequency, non-uniform intensity distribution across the DMD surface owing the Gaussian distribution of the light emitted from the HeNe laser. During scanning, each displayed pattern samples only a local portion of this beam. Consequently, spatial variations in the input intensity produce position-dependent variations of the focal-spot intensity in the sample plane, directly affecting the measurement.

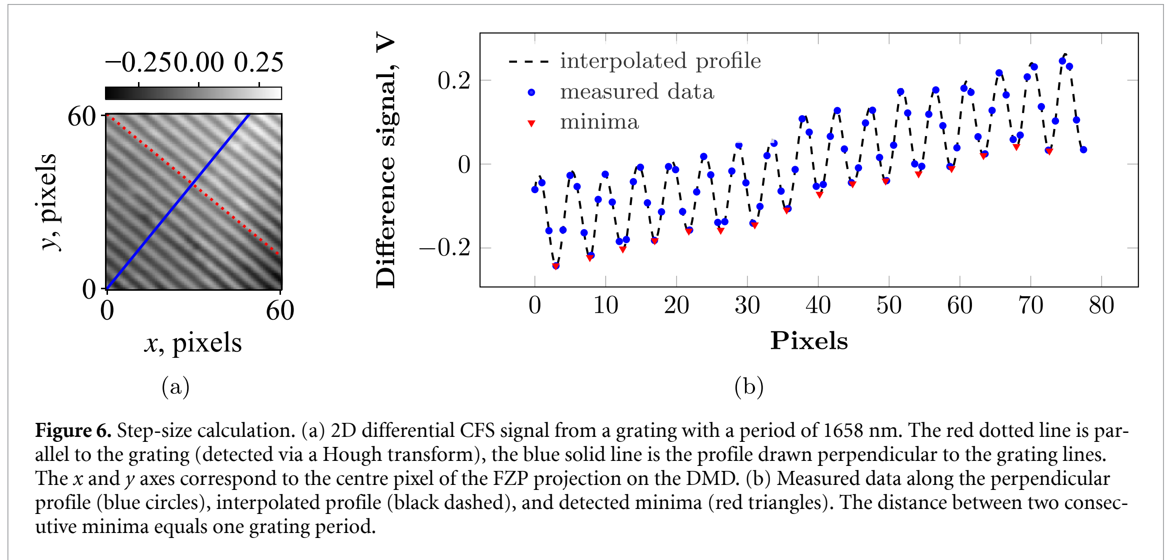

Figure 6. Step-size calculation. (a) 2D differential CFS signal from a grating with a period of 1658 nm. The red dotted line is parallel to the grating (detected via a Hough transform), the blue solid line is the profile drawn perpendicular to the grating lines. The x and y axes correspond to the centre pixel of the FZP projection on the DMD. (b) Measured data along the perpendicular profile (blue circles), interpolated profile (black dashed), and detected minima (red triangles). The distance between two consecutive minima equals one grating period.

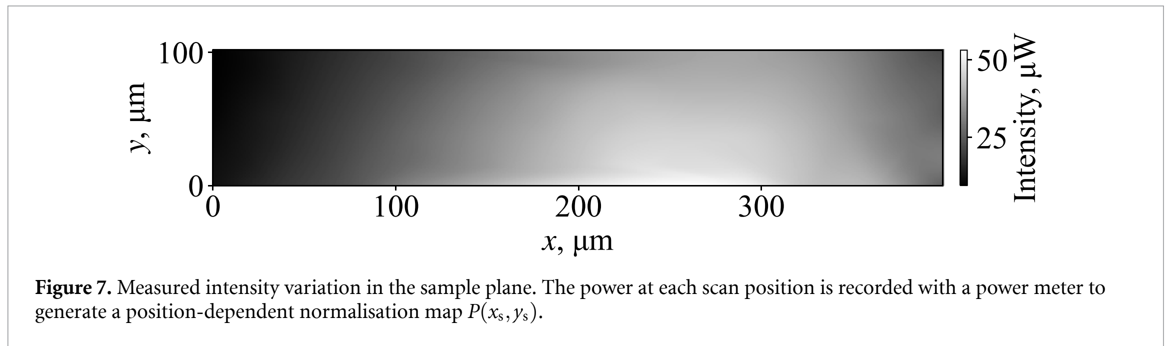

Figure 7. Measured intensity variation in the sample plane. The power at each scan position is recorded with a power meter to generate a position-dependent normalisation map $P(x_s, y_s)$.

To compensate, the intensity distribution is measured in advance and used for a position-dependent normalisation. Within the operating range of input laser power, the differential signal varies linearly with input power, so a simple normalisation using the input power suffices. If $P(x_s, y_s)$ is the measured power map in the sample plane at scan position (x_s, y_s), the corrected signals are,

$$D_1'(x_s, y_s) = \frac{D_1(x_s, y_s)}{P(x_s, y_s)}, \qquad D_2'(x_s, y_s) = \frac{D_2(x_s, y_s)}{P(x_s, y_s)}.$$

$P(x_s, y_s)$ was measured directly using a power meter placed in the focal plane without any sample and the 2D map is shown in figure 7. Across the measured field ($N = 64$ positions), the power ranged from 9.51 µW to 51.4 µW, with a mean of 30.58 µW and standard deviation of 11.27 µW, corresponding to a coefficient of variation of 36.84%, indicating substantial non-uniformity.

The measured non-uniformity reflects the laser beam envelope and system effects such as relay vignetting so the normalisation compensates for their combined influence. To guard against temporal drift, it is advisable to re-measure the power variation every day before actual sample measurements.

4.3. Aberration correction

Field-dependent aberration correction was implemented by iteratively optimising Zernike mode coefficients (Noll indexing) [48]. Coefficients are reported in units of wavelength for the illumination wavelength λ. In the optimisation, the first 14 Zernike modes were included (excluding piston, tip, and tilt). As the DMD provides only binary amplitude modulation, the encoded wavefront exhibits a non-zero residual phase error and modal cross-talk exist, particularly for higher-order modes. As quantified in appendix D via the residual phase error and the cross-talk matrix, this limits the fidelity and marginal benefit of high-order aberration correction in the present implementation. Accordingly, our optimisation focuses on low-order Zernike modes, for which the largest improvements in spot metrics are observed, while higher-order modes provide diminishing returns.

In the first pass, each coefficient was varied between −2 to 2 in steps of 0.1. Successive passes reduced the range and step size by half. The optimisation was implemented as a two-loop process: the outer loop controlled the total number of passes over the selected modes, while the inner loop optimised

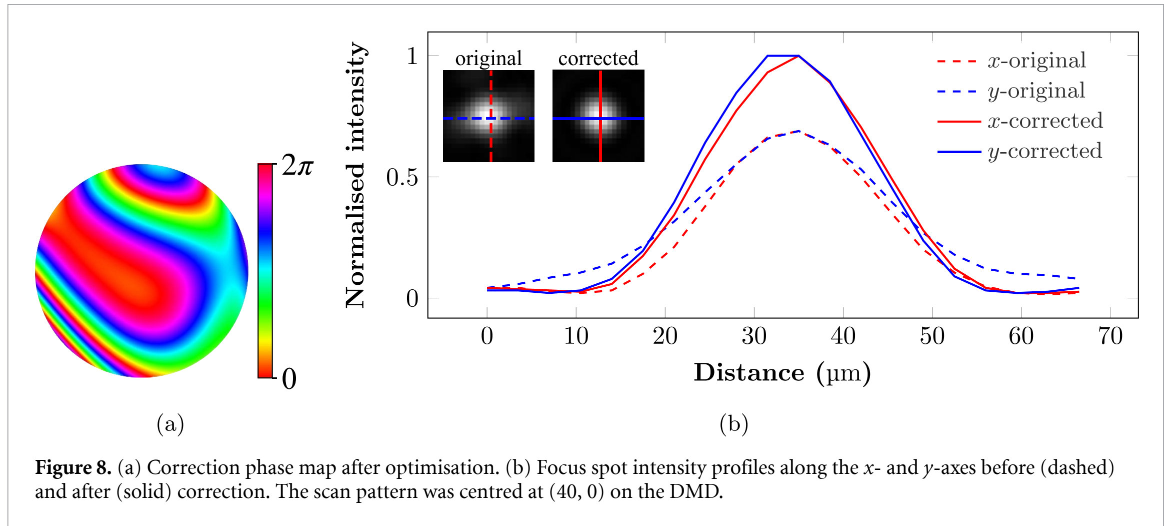

Figure 8. (a) Correction phase map after optimisation. (b) Focus spot intensity profiles along the x- and y-axes before (dashed) and after (solid) correction. The scan pattern was centred at (40, 0) on the DMD.

each aberration sequentially. Once an aberration coefficient was determined, it was kept fixed while the next mode was optimised. When all selected modes were completed, the process repeated according to the number of passes specified in the outer loop, with the reduced coefficient range and step size in each iteration.

A camera conjugate to the image plane, located at the focal plane of lens L5 (see figure 4(a)), is used to record the resulting focus spot. Spot intensity and shape are quantified by fitting a two-dimensional Gaussian distribution to each image after mean-background subtraction. The peak of the fitted Gaussian is evaluated as a function of the Zernike coefficient, and the coefficient that maximises the peak is taken as the optimal value for that mode. This procedure is repeated for each scan coordinate to determine the aberration correction at every scan position.

To evaluate the effectiveness of the method, quantitative comparisons of the focus spot characteristics before and after optimisation are conducted. A representative example at the scan position $(14.52\,\mu\text{m}, 0)$ in the image plane (pattern centred at $(40, 0)$ on the DMD) is shown in figure 8(b). Figure 8(a) shows the optimised phase map used for correction. The corresponding intensity profiles of the focus spot along the x- and y-axes, before and after aberration correction, are shown in figure 8(b). Before correction, the intensity distribution exhibits noticeable asymmetry and a reduced peak due to aberration-induced wavefront distortion. After correction, the intensity profiles are more symmetric, and the peak intensity increases by 45%. Asymmetry is quantified using full width at half-maximum (FWHM) of the spot as,

$$\epsilon = \frac{|\text{FWHM}_x - \text{FWHM}_y|}{\text{FWHM}_x + \text{FWHM}_y}, \tag{10}$$

where FWHM_x and FWHM_y are the full widths at half maximum along the x and y axes. For the example shown, ϵ decreases from 0.053 to 0.007 after correction.

Figure 9 shows the improvement in focus spot intensity and symmetry after optimisation over a 400×200 DMD-pixel scan area: (a)–(c) focus-spot peak intensity (before optimisation, after optimisation, and after normalisation with input power) and (d)–(e) ϵ (before and after optimisation). The mean improvement in the spot intensity across the area is $205 \pm 115\%$. The coefficient of variation (standard deviation / mean) in the spot intensity across the 2D array before optimisation is 39.42%. The value reduces to 16.13% after optimisation and further reduces to 4.47% after normalisation with input intensity. Similarly, the mean ϵ value reduces from 0.109 to 0.022 after optimisation. More plots regarding the algorithm convergence, coefficient fitting and the spatial variation of the retrieved optimum coefficients are included in the supplementary data.

The optimisation primarily improves probe uniformity across the scan field. This is expected to reduce scan-position-dependent aberrations and associated variability in the measured scatterometric signals, thereby lowering measurement uncertainty. However, the present study does not provide a direct quantification of the resulting improvement in parameter-estimation accuracy. Quantifying the impact on reconstruction accuracy is therefore left to future work.

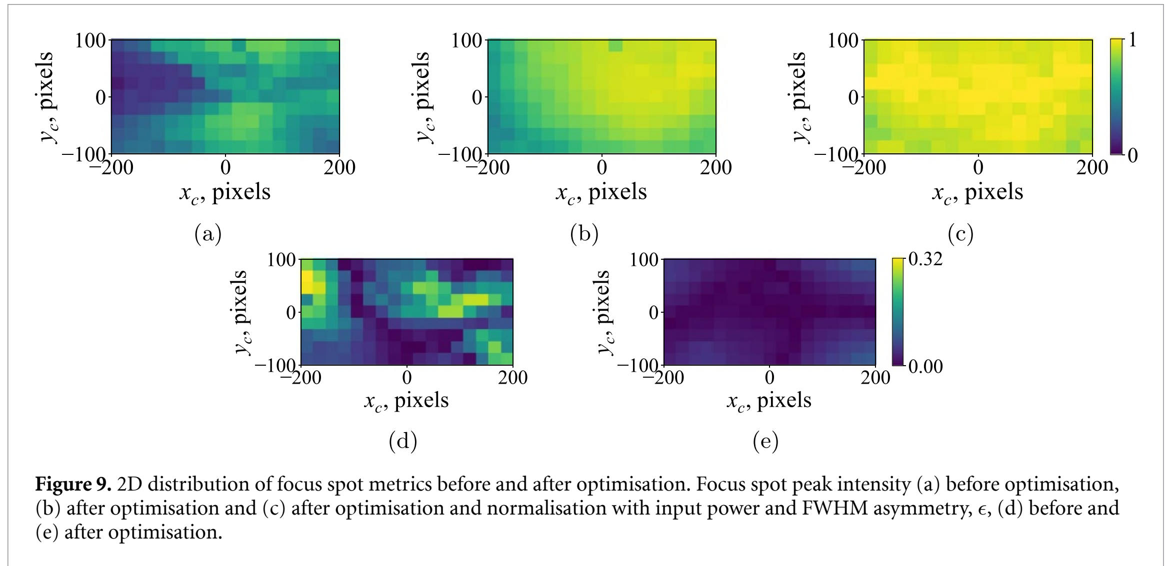

Figure 9. 2D distribution of focus spot metrics before and after optimisation. Focus spot peak intensity (a) before optimisation, (b) after optimisation and (c) after optimisation and normalisation with input power and FWHM asymmetry, ϵ, (d) before and (e) after optimisation.

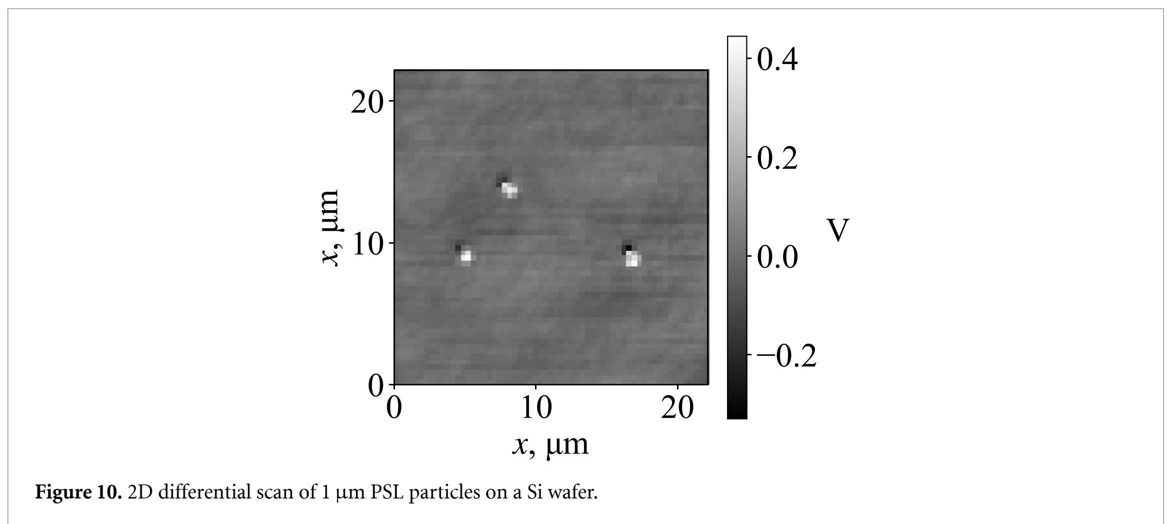

Figure 10. 2D differential scan of 1 µm PSL particles on a Si wafer.

5. Application: particle detection on Si wafer

The performance of the DMD-based CFS system was demonstrated by measuring polystyrene latex (PSL) particles that are randomly deposited on a Si wafer. PSL standards are routinely employed to benchmark contamination-detection sensitivity, and their scattering response approximates that of typical insulating residues encountered on wafers. Figure 10 shows the 2D differential scan map of a Si wafer with 1 µm PSL particles. The signal-to-noise ratio (SNR) of the differential signal was measured to be 16.04 ± 1.11 dB, following the definition $\mathrm{SNR} = 20\log_{10}\left(\frac{V_{\mathrm{signal}}}{V_{\mathrm{noise}}}\right)$.

6. Uncertainty assessment

This section details the measurement uncertainty contributions from the different system components. Table 2 lists the different error sources for a measured differential signal with 1 V peak-to-peak.

- Detector: The dark noise of the detector is measured with the detector switched on but no light incident on the bi-cell. The measured value is 0.927 mV for a detection bandwidth of 300 kHz. This includes the noise from the ADC (analog-to-digital converter) as well.
- Laser: The laser used in the scan head is not intensity stabilised and may have fluctuations in the output power. The mean laser intensity was measured to be 19.2 mW with a standard deviation of 65.2 µW. The value was calculated from a 1-minute measurement of the laser intensity using a power meter, two hours after the laser is switched on. The duration of the measurement corresponds to the

Table 2. Uncertainty budget entries reported as standard uncertainties ($k = 1$) for a measured differential signal of 1 V peak-to-peak. The combined standard uncertainty is computed by calculating the root sum square (RSS) assuming no correlations. A conservative bound assuming full positive correlation between DMD stability and illumination non-uniformity is also shown.

Source	Type [49]	Uncertainty in V
Detector	A	9.27×10^{-4} V
Laser	A	3.38×10^{-3} V
DMD pointing stability	A	0.0565 V
Illumination non-uniformity (post aberration-correction and power-normalisation)	A	0.045 V
Sample tilt (normal distribution, $k = 1$)	B	0.0236 V
Total (uncorrelated, RSS)		0.0761 V
Total (full positive correlation between DMD stability and illumination non-uniformity)		0.104 V

duration of a typical scan. The signal varies linearly as a function of laser intensity and can differ by 0.338% from the mean value.

- DMD: The pointing stability of the DMD was measured by placing the quadrant detector directly in the sample plane and recording the difference signal as a function of time. The difference signal was normalised by the total power to account for variation in input power. Ideally, the signal should be zero and remain constant with time, and any deviations indicate drift or disturbances to the setup. The standard deviations of the two difference signals, D_1' and D_2', for 2 min measurements are 0.051 V and 0.024 V, respectively. These values can be added as absolute uncertainty contributions to all measurements. Additionally, the non-uniformity in the focal-plane intensity distribution further adds to the uncertainty. This variation was measured to be 4.47% of the mean value after aberration correction and output-power normalisation. It is possible that correlations exist between DMD pointing stability and focal-spot non-uniformity and a conservative uncertainty estimate including the correlation has been added in table 2.
- Sample tilt: The influence of sample tilt on the measurement uncertainty has been discussed in detail in our previous work [14]. Assuming the sample tilt to be less than $\pm 1\lambda$, an uncertainty of 2.36% is added.

7. Discussion

In this work, a DMD-based scanning system for a CFS setup is presented. An FZP pattern is projected on the DMD and sequentially shifted to scan the focus spot in the sample plane. To the best of our knowledge, this is the first CFS implementation in which lateral scanning is realised using a DMD. The setup has no macroscopic moving components reducing mechanical vibrations. The high switching rate of the DMD also enables fast scanning. The setup used a switching rate of 250 Hz as the patterns were in 8-bit format. 1-bit encoding should enable faster scans up to 17 kHz. A comparison of the performance parameters of the DMD-based system to the piezo-based baseline CFS system is detailed in table 3.

The measurement protocol takes into account issues such as non-uniform intensity of the incident beam as well as the intrinsic problem of field-dependent, off-axis beam aberrations associated with beam scanning approaches. An iterative optimisation algorithm is used to project aberration corrected scan patterns on the DMD, combining both scanning and aberration correction and improving PSF uniformity over the scan area. The system performance was demonstrated for detection of particle contamination on a Si wafer. These results show the potential of the system for applications in sub-wavelength contamination detection and nanostructure metrology. Although we demonstrate substantial improvements in probe uniformity, we do not perform a reconstruction-based comparison (with and without aberration correction) of recovered sample parameters in this manuscript. Therefore, the results should not be interpreted as a demonstrated improvement in reconstruction accuracy, rather, they establish the DMD-FZP scan head and its calibration workflow as a high-throughput CFS platform on which such reconstruction-based metrological validation can be carried out in future work.

Despite the advantages, the biggest drawback of the technique is the low power efficiency. The use of an FZP pattern over single pixel scanning improves the efficiency but is still limited to 1.6%.

Table 3. Comparison of the performance parameters of CFS systems using DMD-based scanning using FZP projection versus piezo-based translation stage.

	Scanning strategies	
Metric	DMD (DLP9500)	Piezo (P-625.2 CD)
Scan trajectory	Raster scan (FZP projection)	Triangular
Scan range	401.8 μm × 96.9 μm	500 μm × 500 μm
Scan speed	∼6.5 mm s^{-1} [a]	∼167 μm s^{-1} [b]
Minimum pixel size	0.363 μm	1.4 nm
Numerical aperture (NA)	0.4	0.4
Laser wavelength	632.8 nm	632.8 nm
Laser power at sample	480 μW	68 μW
Measurement uncertainty[c]	76.1 mV	23.63 mV
Throughput[d]	∼4.25 s	∼460 s

[a] Calculated for highest 1-bit refresh rate of 17 857 Hz.
[b] 1/35 of the first resonant frequency of the piezo (P-625.2 CD).
[c] 1σ measured at 1 V_{pp}. Does not include surface roughness.
[d] Area of 100 μm × 100 μm. Pixel size fixed to the DMD minimum of 0.363 μm.

Parallel operation follows naturally by displaying an array of FZPs (or selected diffraction orders) to create multiple foci, each with its own binary correction pattern, enabling near-linear gains in scan speed within the available optical power. Compared to piezo-based scanning, the DMD-based approach improves scan throughput, while the position-dependent correction compensates for the off-axis aberrations inherent to beam scanning (as encountered in galvo-based scanning). The throughput can be further improved using parallel scanning.

Acknowledgments

We thank Roland Horsten for his help with design and development of the quadrant detector and Thim Zuidwijk for the support on the opto-mechanical components used in the setup. We also thank Thomas Siefke for the grating sample fabrication as part of beCoMe project. We acknowledge the use of AI-assisted tools, including language and grammar checking software, to improve the clarity and readability of the manuscript.

Data availability statement

The data that support the findings of this study are openly available at the following URL/DOI: https://doi.org/10.4121/e62d520c-d7b1-4ef6-a8b0-a90d588c4d5e.v1 [50].

Supplementary Data

This appendix supplements subsection 4.3 by providing additional details of the aberration-correction procedure implemented with binary amplitude modulation on a DMD, with the goal of improving focus-spot uniformity across the scan field. Because the DMD provides only binary amplitude modulation, both the diffraction efficiency and the phase fidelity of the encoded wavefront are fundamentally limited compared with the multi-level phase modulation.

A. Diffraction efficiency penalty of binary amplitude modulation

Figure 11 compares the fraction of power enclosed within the first Airy disk of the focused spot to the total incident power for: (i) an ideal continuous-phase lens, (ii) a phase-only element quantised to L discrete levels, and (iii) binary amplitude modulation (DMD). As expected, the enclosed-power fraction increases monotonically with the number of phase levels and approaches the continuous-phase limit. By contrast, the binary-amplitude case remains substantially lower, which directly contributes to the low overall optical throughput of the present implementation.

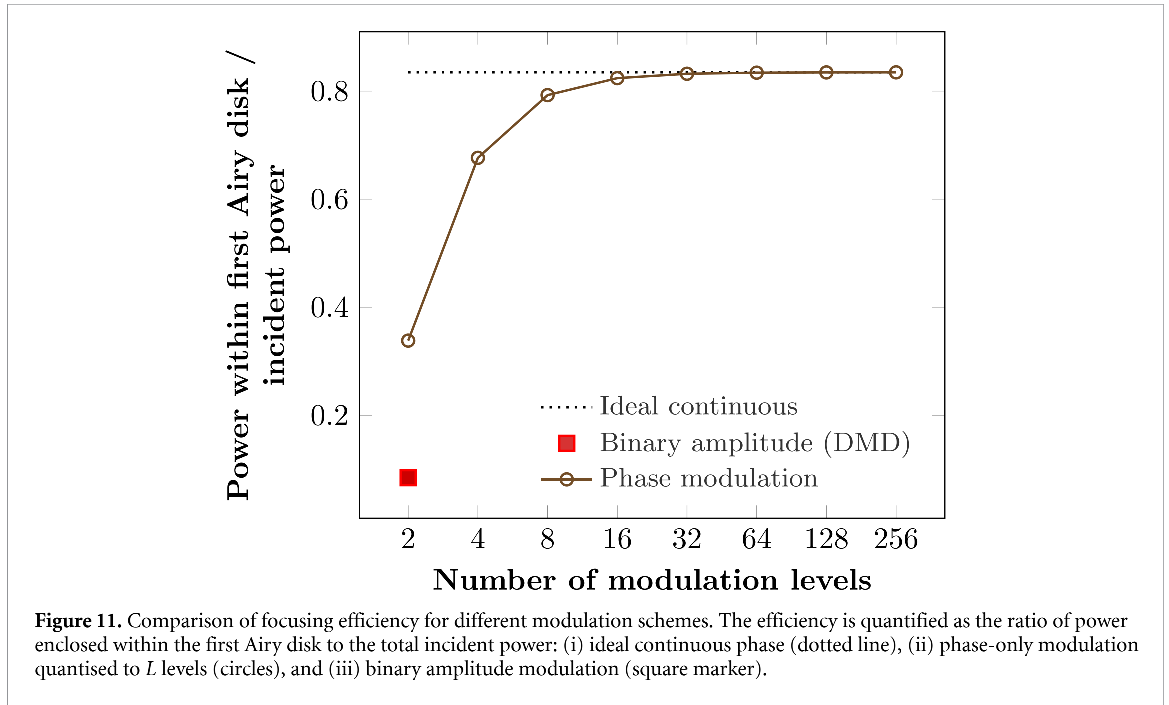

Figure 11. Comparison of focusing efficiency for different modulation schemes. The efficiency is quantified as the ratio of power enclosed within the first Airy disk to the total incident power: (i) ideal continuous phase (dotted line), (ii) phase-only modulation quantised to L levels (circles), and (iii) binary amplitude modulation (square marker).

B. Zernike coefficient optimisation and convergence diagnostics

During optimisation, at each scan coordinate, individual Zernike coefficients C_n^m (Noll indexing, units of waves at $\lambda = 632.8$ nm) were swept while imaging the focus spot on a camera conjugate to the sample plane. The merit function was the fitted peak intensity. In addition, the fitted FWHM along x and y and the asymmetry metric ϵ (defined in the main text) were recorded.

Figure 12 shows the evolution of these metrics over one optimisation pass. Figure 13 shows example coefficient sweeps (blue markers) together with Gaussian fits used to estimate the optimal C_n^m (black dashed curves). Figure 14 shows example 2D maps of retrieved coefficients across the field of view. Unless stated otherwise, piston, tip, and tilt were excluded and the first 14 non-trivial modes were considered.

C. Repeatability and noise sensitivity

To quantify convergence repeatability under nominally identical conditions, we performed 10 independent optimisations per mode and computed the run-to-run variation of the retrieved coefficient. For the low-order modes $(n,m) = (2,0)$, $(2,2)$, and $(2,-2)$, the per-run RMS coefficient variations relative to the mean are 0.1484, 0.0430, and 0.0431 waves, respectively (coefficients in waves at $\lambda = 632.8$ nm). We restrict this repeatability analysis to the low-order modes because, as seen in figure 12, higher-order modes yield only marginal improvement in the spot metrics.

The sensitivity of the Zernike optimisation to measurement noise is primarily determined by (i) the noise on the merit function (the fitted peak intensity), and (ii) the local curvature of the merit-function landscape around the optimum for each mode. In our implementation the feedback signal is obtained from a 2D Gaussian fit to the measured spot image after background subtraction, which suppresses pixel-scale camera noise compared with single-pixel peak metrics. In addition, frame averaging is used in the camera acquisition (effective $\sim$1 s per image) to reduce random measurement noise.

To quantify the local noise sensitivity, we fit a parabola $I(C) = \alpha C^2 + \beta C + \gamma$ to the samples in the neighbourhood of the maximum, I is the intensity of the fitted peak and C is the coefficient of the Zernike mode. Assuming additive Gaussian noise on the measured peak intensity, $I_{\text{measured}}(C) = I(C) + \epsilon$, $\epsilon \sim \mathcal{N}(0, \sigma_I^2)$, the coefficient uncertainty is obtained from the local curvature at the optimum. Since the fit is performed around a maximum, the quadratic coefficient is negative ($\alpha < 0$), we use the curvature magnitude $|\alpha|$ and obtain

$$\sigma_C = \sqrt{\frac{\sigma_I}{|\alpha|}}, \tag{11}$$

where σ_C and σ_I represent the standard deviation of the retrieved Zernike mode coefficient and the measured peak intensity values respectively. Table 4 summarises the noise sensitivity statistics for selected

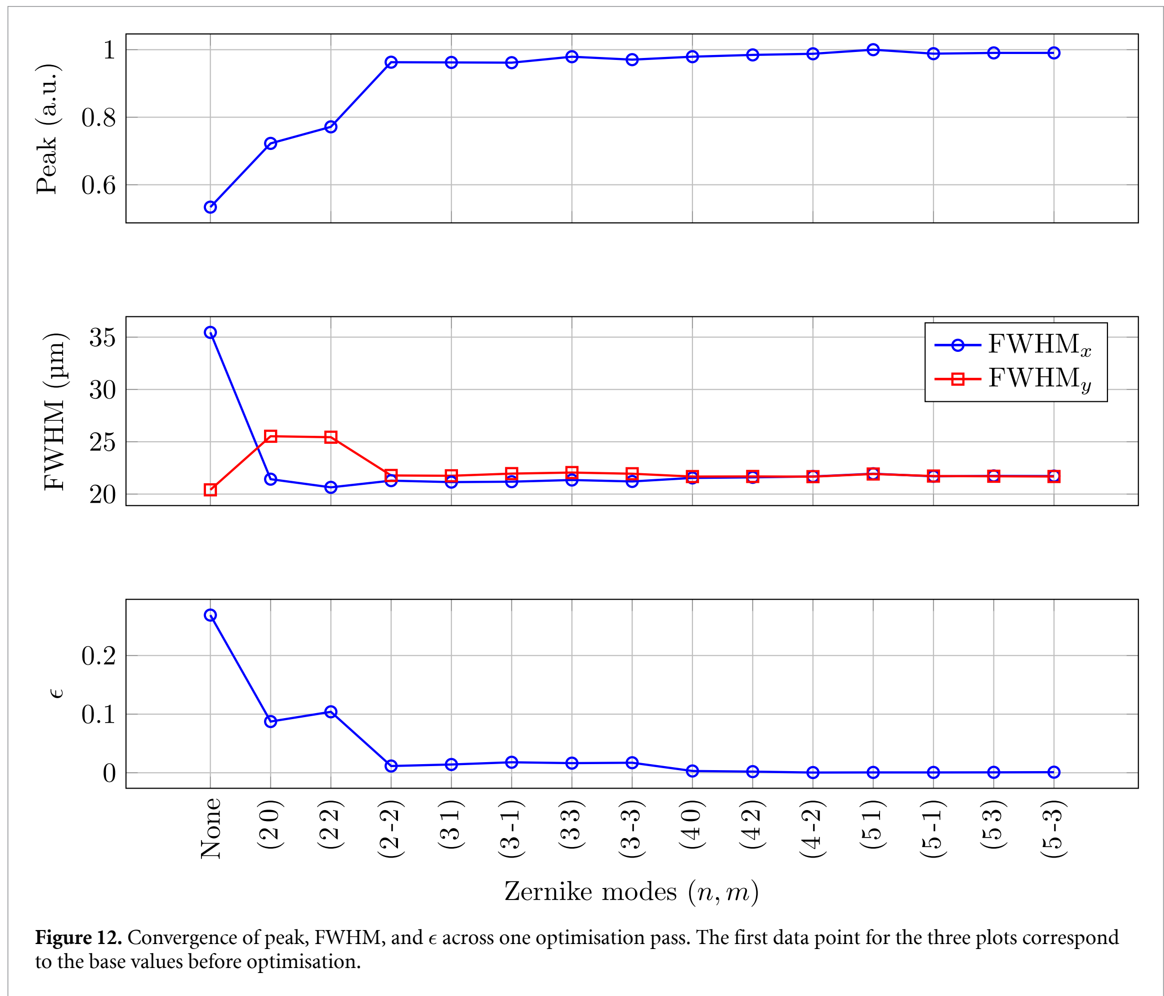

Figure 12. Convergence of peak, FWHM, and ϵ across one optimisation pass. The first data point for the three plots correspond to the base values before optimisation.

Zernike modes. The curvature magnitude $|\alpha|$ for each mode is reported as the mean value over six independent measurements. We compute σ_C assuming an 8-bit camera (0–255) and a representative peak-intensity noise of $\sigma_I = 5$. For the modes reported here, the higher-order modes ($n = 4$) have larger $|\alpha|$ values, which leads to reduced noise sensitivity (smaller σ_C) under the same assumed σ_I.

D. Phase fidelity

In the experiments, optimisation progress was quantified using focal-spot metrics, while the corrected wavefront phase was not measured directly. To estimate the residual phase error introduced by binary amplitude encoding, a numerical study of the full encoding-propagation-filtering process was performed. In the simulation, a uniform input field was incident on the DMD. A binarised mask encoding the desired phase profile (combined effect of the focusing element and an individual Zernike mode) was displayed on the DMD. After Fourier filtering and focusing, the beam was re-collimated and the complex field was evaluated in the pupil plane (front focal plane of the collimating lens). The achieved phase $\phi_{\text{enc}}(x,y)$ was then compared to the target phase $\phi_{\text{tar}}(x,y)$ and the residual phase error was computed as a standard deviation over the pupil,

$$\Delta\phi_{\text{RMS}} = \sqrt{\langle(\phi_{\text{enc}} - \phi_{\text{tar}}) - \langle\phi_{\text{enc}} - \phi_{\text{tar}}\rangle\rangle^2}, \tag{12}$$

where $\langle\cdot\rangle$ denotes an average over the pupil. The residual phase error is plotted in figure 15. In addition, phase fidelity was quantified by analysing how the encoded wavefront energy is distributed among Zernike modes for each projected mode. The resulting cross-talk matrix (heatmap in figure 16) shows that, while high-order modes can be generated (diagonal response), binary encoding introduces substantial cross-talk. Energy from a desired high-order mode is redistributed predominantly into modes with the same azimuthal order m but lower radial order. In the present application, this behaviour has limited impact because the largest improvements in focus-spot uniformity are obtained from the first few modes, and higher-order modes contribute only marginal additional benefit.

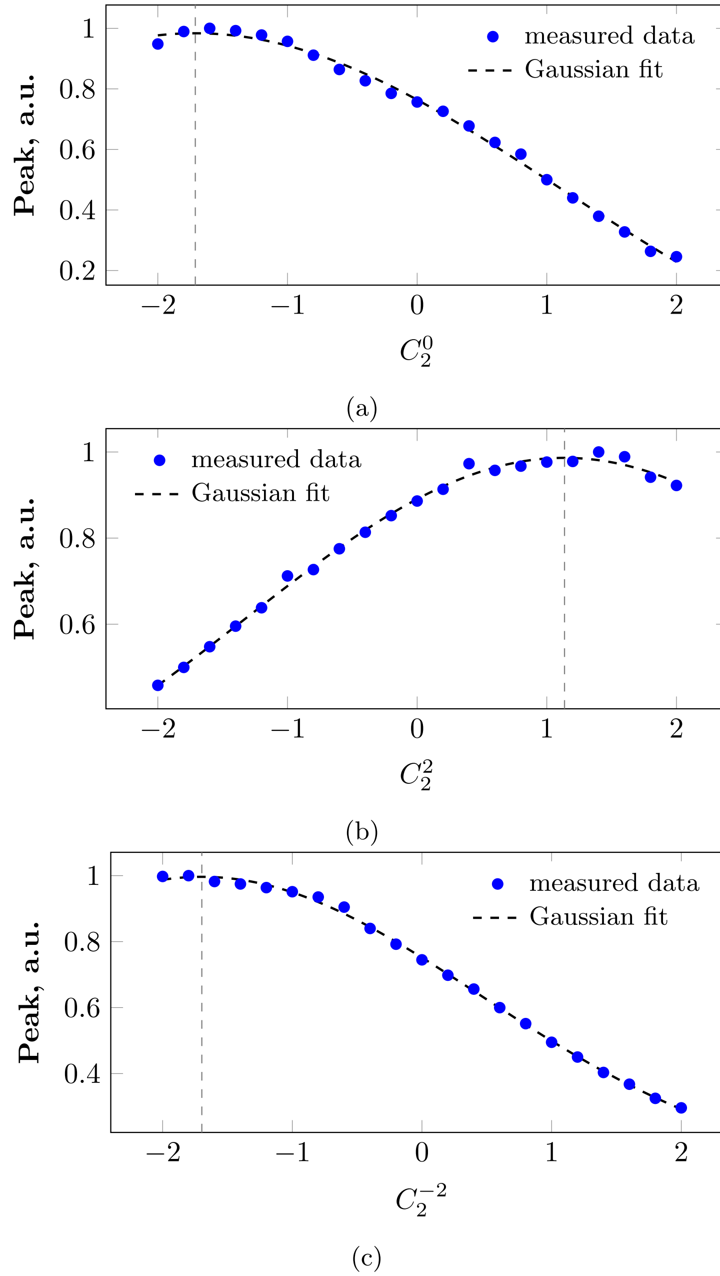

Figure 13. Measured peaks vs. coefficient (blue markers), Gaussian fits (black dashed), and optimal coefficient (grey line) for (a) defocus (Z_2^0), (b) astigmatism (Z_2^2), and (c) oblique astigmatism aberrations. The peaks correspond to the maximum intensity of the focus spot captured using a CCD camera.

Table 4. Noise sensitivity statistics for selected Zernike modes from six independent measurements. $|\alpha|$ is the mean fitted curvature magnitude, σ_C is computed assuming $\sigma_I = 5$ and is reported in waves ($\lambda = 632.8$ nm).

(n, m)	$\lvert\alpha\rvert$	σ_C
(2,−2)	16.615 618	0.5485
(2, 0)	39.300 401	0.3567
(2, 2)	16.645 943	0.5481
(4,−2)	72.563 953	0.2625
(4, 0)	167.144 182	0.1730
(4, 2)	77.405 016	0.2542

Figure 14. The 2D heatmap of the optimal coefficients for (a) defocus (Z_2^0), (b) astigmatism (Z_2^2), and (c) oblique astigmatism aberrations.

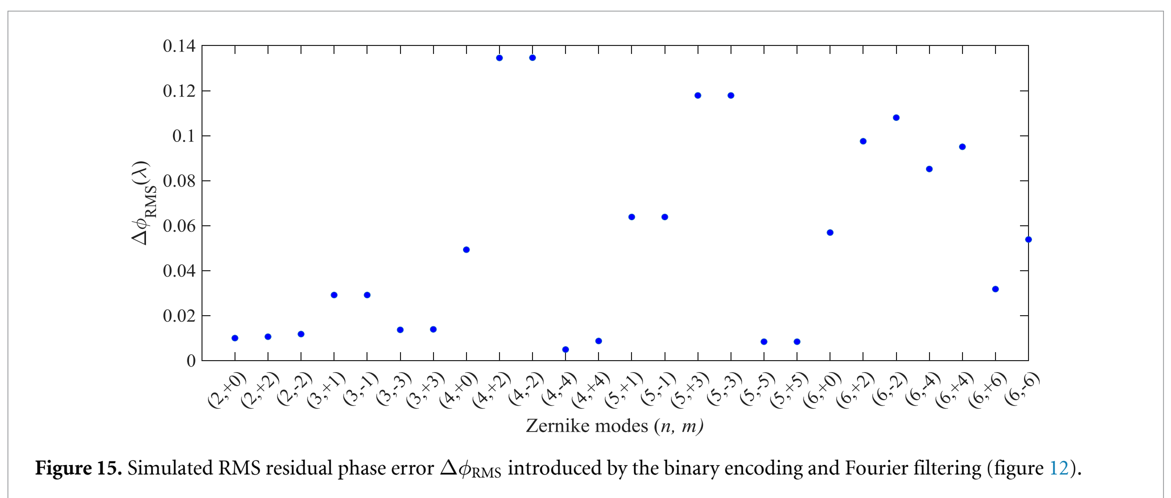

Figure 15. Simulated RMS residual phase error $\Delta\phi_{RMS}$ introduced by the binary encoding and Fourier filtering (figure 12).

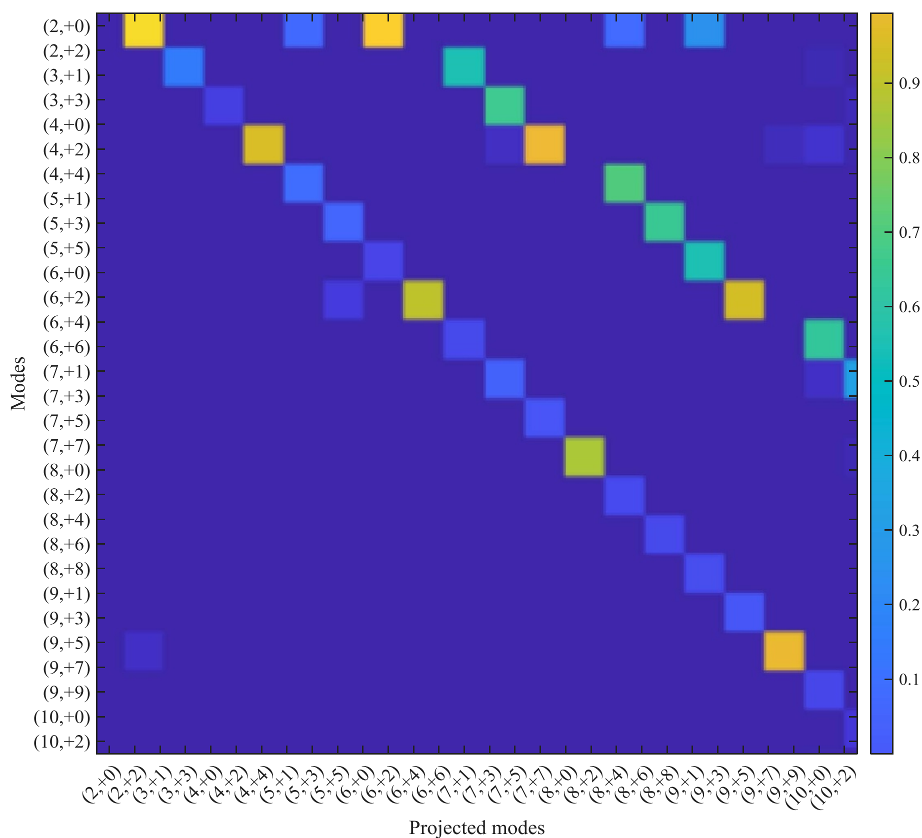

Figure 16. Modal cross-talk matrix showing the energy fraction recovered in each Zernike component when encoding a single target mode (columns: projected mode, rows: recovered mode).

Funding

We acknowledge the Nederlandse Organisatie voor Wetenschappelijk Onderzoek (Project 17-24 Synoptics No.2) for funding this research.

Author contributions

Sarika Soman 0000-0002-8316-8639
Formal analysis (lead), Investigation (lead), Methodology (lead), Visualization (lead), Writing – original draft (lead)

Eren Özdemir
Investigation (supporting), Software (equal), Validation (equal), Writing – review & editing (equal)

Silvania Pereira 0009-0001-9148-1975
Conceptualization (equal), Funding acquisition (lead), Resources (lead), Supervision (lead), Writing – review & editing (equal)

References

[1] Archenti A, Gao W, Donmez A, Savio E and Irino N 2024 Integrated metrology for advanced manufacturing *CIRP Ann.* **73** 639–65
[2] Orji N *et al* 2018 Metrology for the next generation of semiconductor devices *Nat. Electron.* **1** 532–47
[3] Bergmann R B, Kalms M and Falldorf C 2021 Optical in-process measurement: concepts for precise, fast and robust optical metrology for complex measurement situations *Appl. Sci.* **11** 10533
[4] Nouri M *et al* 2025 Resolution enhancement methods in optical microscopy for dimensional optical metrology *J. Eur. Opt. Soc.: Rapid Publ.* **21** 7
[5] Shimizu Y, Chen L-C, Kim D W, Chen X, Li X and Matsukuma H 2021 An insight into optical metrology in manufacturing *Meas. Sci. Technol.* **32** 042003
[6] Kumar N, Petrik P, Ramanandan G K P, Gawhary O E, Roy S, Pereira S F, Coene W M J and Urbach H P 2014 Reconstruction of sub-wavelength features and nano-positioning of gratings using coherent Fourier scatterometry *Opt. Express* **22** 24678–88

[7] Menzel M and Pereira S F 2020 Coherent Fourier scatterometry reveals nerve fiber crossings in the brain *Biomed. Opt. Express* **11** 4735–58
[8] Rafighdoost J, Kolenov D and Pereira S F 2024 Coherent Fourier scatterometry for detection of killer defects on silicon carbide samples *IEEE Trans. Semicond. Manuf.* **37** 124–8
[9] Roy S, Assafrao A C, Pereira S F and Urbach H P 2014 Coherent Fourier scatterometry for detection of nanometer-sized particles on a planar substrate surface *Opt. Express* **22** 13250–62
[10] Paul A, Wever R, Soman S and Pereira S F 2025 Utilizing focused field as a probe for shape determination of subwavelength structures via coherent Fourier scatterometry *Phys. Rev. Appl.* **23** 024016
[11] Kolenov D, Davidse D, Cam J L and Pereira S F 2020 Convolutional neural network applied for nanoparticle classification using coherent scatterometry data *Appl. Opt.* **59** 8426–33
[12] Soman S, Velt B I, Horsten R and Pereira S F 2025 Coherent Fourier scatterometry using rotational scanning *Opt. Eng.*, **64** 074106
[13] Soman S, Horsten R, Scholte T and Pereira S F 2024 Multi-beam coherent fourier scatterometry *Meas. Sci. Technol.* **35** 075905
[14] Soman S, Horsten R and Pereira S F 2025 High-speed coherent Fourier scatterometry: galvo mirror integration for fast surface inspection *Measurement* **258** 119294
[15] Refai H H, Sluss J J Jr and Tull M P 2007 Digital micromirror device for optical scanning applications *Opt. Eng.* **46** 085401
[16] Cheng J, Gu C, Zhang D, Wang D and Chen S-C 2016 Ultrafast axial scanning for two-photon microscopy via a digital micromirror device and binary holography *Opt. Lett.* **41** 1451–4
[17] Wang Q, Zheng J, Wang K, Gui K, Guo H and Zhuang S 2016 Parallel detection experiment of fluorescence confocal microscopy using DMD *Scanning* **38** 234–9
[18] Li S and Liang R 2020 DMD-based three-dimensional chromatic confocal microscopy *Appl. Opt.* **59** 4349–56
[19] Dan D *et al* 2013 DMD-based LED-illumination super-resolution and optical sectioning microscopy *Sci. Rep.* **3** 1116
[20] Li M *et al* 2020 Structured illumination microscopy using digital micro-mirror device and coherent light source *Appl. Phys. Lett.* **116** 233702
[21] Smith B, Hellman B, Gin A, Espinoza A and Takashima Y 2017 Single chip lidar with discrete beam steering by digital micromirror device *Opt. Express* **25** 14732–45
[22] Rodriguez J, Smith B, Hellman B and Takashima Y 2020 Fast laser beam steering into multiple diffraction orders with a single digital micromirror device for time-of-flight lidar *Appl. Opt.* **59** G239–48
[23] Rueda H, Arguello H and Arce G R 2014 DMD-based implementation of patterned optical filter arrays for compressive spectral imaging *J. Opt. Soc. Am. A* **32** 80–89
[24] Sun A *et al* 2017 Optical scanning holography based on compressive sensing using a digital micro-mirror device *Opt. Commun.* **385** 19–24
[25] Kuang C, Ma Y, Zhou R, Lee J, Barbastathis G, Dasari R R, Yaqoob Z and So P T C 2015 Digital micromirror device-based laser-illumination Fourier ptychographic microscopy *Opt. Express* **23** 26999–7010
[26] Sun A, He X, Kong Y, Cui H, Song X, Xue L, Wang S and Liu C 2017 Ultra-high speed digital micro-mirror device based ptychographic iterative engine method *Biomed. Opt. Express* **8** 3155–62
[27] Ren M, Chen J, Chen D and Chen S-C 2020 Aberration-free 3D imaging via DMD-based two-photon microscopy and sensorless adaptive optics *Opt. Lett.* **45** 2656–9
[28] Wang Y, Li H, Hu Q, Cheng X, Chen R, Lv X and Zeng S 2020 Aberration-corrected three-dimensional non-inertial scanning for femtosecond lasers *Opt. Express* **28** 29904–17
[29] Pozzi P, Wilding D, Soloviev O, Verstraete H, Bliek L, Vdovin G and Verhaegen M 2017 High speed wavefront sensorless aberration correction in digital micromirror based confocal microscopy *Opt. Express* **25** 949–59
[30] Singh K, Dudley A and Forbes A 2023 Versatile all-digital transport-of-intensity based wavefront sensor and adaptive optics using a dmd *Opt. Express* **31** 8987–97
[31] Zhang Q, Hu Q, Berlage C, Kner P, Judkewitz B, Booth M and Ji N 2023 Adaptive optics for optical microscopy *Biomed. Opt. Express* **14** 1732–56
[32] Benton D 2021 Aberration and coherence effects with a micromirror array *Technologies for Optical Countermeasures Xviii and High-Power Lasers: Technology and Systems, Platforms, Effects V* vol 11867 (SPIE) pp 59–69
[33] Zandi M, Benton D and Sugden K 2023 Laser beam wavelength determination algorithm using a digital micromirror device *Opt. Eng.* **62** 064101
[34] Booth M J 2007 Adaptive optics in microscopy *Philos. Trans. R. Soc. A* **365** 2829–43
[35] Booth M J 2014 Adaptive optical microscopy: the ongoing quest for a perfect image *Light Sci. Appl.* **3** e165
[36] Goodman J W 2005 *Introduction to Fourier Optics* (Roberts and Company Publishers)
[37] Zhang Y, Strube S, Molnar G, Danzebrink H U, Dai G, Bosse H and Hou W 2013 Parallel large-range scanning confocal microscope based on a digital micromirror device *Optik* **124** 1585–8
[38] Jang J, Kim W, Oh J S, Kim S-W and Kim Y-J 2022 Fast and precise laser beam scanning by nonperiodic grating on a binary micromirror array *Opt. Eng.* **61** 061412
[39] Benton D M 2018 Multiple beam steering using dynamic zone plates on a micromirror array *Opt. Eng.* **57** 073109
[40] Cao Q and Jahns J 2004 Comprehensive focusing analysis of various Fresnel zone plates *J. Opt. Soc. Am. A* **21** 561–71
[41] Lindle J R and Watnik A T 2018 Large angle nonmechanical laser beam steering at 4.6 um using a digital micromirror device *Opt. Eng.* **57** 027108
[42] Young M 1972 Zone plates and their aberrations *J. Opt. Soc. Am.* **62** 972–6
[43] Fukutake N 2020 A general theory of far-field optical microscopy image formation and resolution limit using double-sided Feynman diagrams *Sci. Rep.* **10** 17644
[44] Sheppard C and Cogswell C 1990 Three-dimensional image formation in confocal microscopy *J. Microsc.* **159** 179–94
[45] Bouwhuis G and Spruit J 1990 Optical storage read-out of nonlinear disks *Appl. Opt.* **29** 3766–8
[46] Soman S and Pereira S F 2025 Aberration characterisation in coherent Fourier scatterometry *Proc. SPIE* **13567** 135672J
[47] Texas Instruments DMD optical efficiency for visible wavelengths *Rev. B.*(available at: www.ti.com/lit/pdf/DLPA083)
[48] Noll R J 1976 Zernike polynomials and atmospheric turbulence* *J. Opt. Soc. Am.* **66** 207–11
[49] BIPM, IEC, IFCC, ILAC, ISO, IUPAC, IUPAP and OIML 2008 Evaluation of measurement data - Guide to the expression of uncertainty in measurement *Joint Committee for Guides in Metrology, JCGM* **100**
[50] Soman S, Özdemir E and Pereira S Dataset accompanying the publication: "Scanning in coherent Fourier scatterometry using Fresnel zone plate projection on a digital micro-mirror device" *4TU.ResearchData.* (https://doi.org/10.4121/e62d520c-d7b1-4ef6-a8b0-a90d588c4d5e.v1)